

Nanopattern formation in self-assembled monolayers of thiol-capped Au nanocrystals

R. Banerjee, S. Hazra, S. Banerjee, and M. K. Sanyal

Surface Physics Division, Saha Institute of Nuclear Physics, 1/AF Bidhannagar, Kolkata 700 064, India

(Received 10 September 2008; revised manuscript received 3 August 2009; published 9 November 2009)

The structure and the stability of the transferred monolayers of gold-thiol nanoparticles, formed at air-water interface at different surface pressure, on to silicon surface have been studied using two complementary techniques, x-ray reflectivity and atomic force microscopy (AFM). Networklike nanopatterns, observed through AFM, of the in-plane aggregated nanoparticles can be attributed to the late stage drying of the liquid trapped in the islands formed by nanoparticles. During drying process the trapped liquid leaves pinholes in the islands which by the process of nucleation and growth carry the mobile nanoparticles on their advancing fronts such that the nanoparticles are trapped at the boundaries of similar adjacent holes. This process continues bringing about in-plane as well as out-of-plane restructuring in the monolayer until the liquid evaporates completely rendering a patterned structure to the islands and instability in the monolayer is then stabilized.

DOI: [10.1103/PhysRevE.80.056204](https://doi.org/10.1103/PhysRevE.80.056204)

PACS number(s): 81.16.Rf, 81.07.Bc, 68.18.Jk, 68.37.Ps

I. INTRODUCTION

The formation of foamlike or cellular structures of monolayer of organic capped nanoparticles on liquid surfaces and on native oxide terminated silicon substrates has been an area of active research. The tendency of nanoparticles to self-assemble on drying [1] can be exploited to generate well-organized two-dimensional patterns extending from nano to micrometer length scales and opens up possibility of maskless fabrications of nanodevices for future applications. Nanoscale electronic devices are expected to be formed primarily due to covalently linked nanocluster superlattices [2] and have possible applications as sensors and photonic devices [3,4]. The interplay of several interfacial forces [5,6], hydrodynamic mechanisms such as Marangoni-Bénard convection [7–9], spinodal decomposition [10–14], kinetically governed self-assembly [15] and coalescence of nearest nucleation sites [16] are thought to be responsible for driving the assembly of complex, gradually evolving structures or patterns. Interestingly, a number of patterns observed for a large number of different systems, have a striking resemblance in form and structure though these systems have drastically different physical or chemical properties. X-ray reflectivity (XRR) and atomic force microscopy (AFM) techniques provide us important information regarding structure and morphology of deposited monolayer on substrate and on water surface from which the deposition can be carried out by Langmuir-Blodgett (LB) and Langmuir-Schaeffer (LS) techniques [17–22].

Morphology and structure of a deposited monolayer on a substrate exhibit rich variety due to complex nature of morphology of nanoparticle monolayer on water surface that depends on surface pressure, temperature [19] and transfer procedure that involves adhesion, diffusion and drying processes [20]. The motivation of this investigation is to probe the evolution in the structure of the transferred monolayers brought about by drying-mediated self-assembly of nanoparticles, complementarily by time-resolved AFM and XRR measurements. The results of this investigation should also provide information required to understand the interplay of various forces during different stages of “drying” process of

nanoparticle monolayer transferred from water surface to a solid substrate. The growth mechanism of such films transferred from water surface to solid substrate involves diffusion and adsorption processes and have been studied by x-ray scattering and AFM techniques [17]. It is to be noted here that unlike one-dimensional transfer [20] of amphiphilic molecules from horizontal water surface to vertical substrate in LB technique, transfer of spherical nanoparticles with thiol encapsulation on a horizontal substrate in LS technique, drying and draining of water becomes a dominating factor [1]. By tuning the surface pressure used for horizontal deposition in a Langmuir trough, and taking advantage of the fact that the nanocrystals are not chemically attached to the substrate but only adhere weakly, we could study complex pattern formation of nanoclusters.

II. EXPERIMENT

Au nanoparticles, encapsulated with dodecanethiol were synthesized by phase-transfer redox reaction mechanism using Brust method [23]. Methanol was added to the toluene solution, containing the capped nanoparticles to remove excess reagents and the nanoparticles were filtered out from the solution. The particles were then redispersed in toluene and a desired concentration of the nanoparticles (0.25 mg/ml) was obtained. Transmission electron microscopy (TEM) measurements were carried out with a JEOL JEM-2010 microscope operated at 200 kV. Samples for TEM were prepared by lowering the concentration of the nanoparticles in the toluene sol and drop casting on a carbon-coated grid, such that the coverage would be appropriate. The samples were then left to dry out overnight, in a desiccator. Left panel of Fig. 1 shows one representative TEM micrograph. The average diameter of the metallic core of the nanoparticle was determined by the particle size distribution and found to be around 2.9 ± 0.55 nm. The metallic core is encapsulated by thiols of about 1 nm, so the average size of the encapsulated nanocrystal is about 5 nm. UV-VIS measurements (Cintra 10e, GBC) were done and the optical-absorption spectra of the Au sol indicated the characteristic plasmon band at 515 nm (see right panel of Fig. 1). A rough estimate of the size of

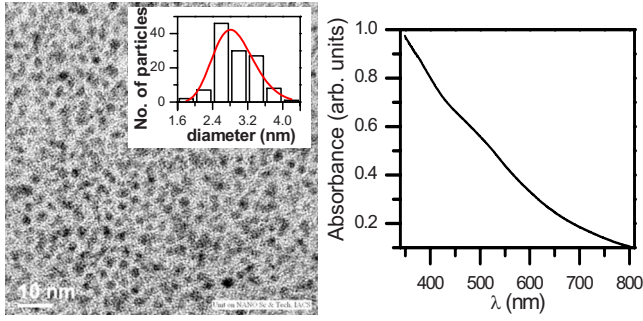


FIG. 1. (Color online) Left panel: typical TEM micrograph with particle size distribution in the inset. The average size of the metallic core of the nanocrystal is 2.9 nm. Right panel: UV-VIS absorption spectra showing plasmon band at around 515 nm.

the nanoparticles from the UV-VIS measurements [24] is quite comparable to that of the TEM measurements. A 1500 μL aliquot of the toluene solution of the Au nanoparticles (0.25 mg/ml) was then spread uniformly using a micropipette on the surface of the Milli-Q water (Milipore) in a Langmuir trough (KSV 5000). It was kept undisturbed for some time to let the solvent evaporate and the hydrophobic dodecanethiol encapsulated Au particles lay suspended at the air-water interface [17]. A pressure-area (π - A) isotherm was recorded at 18 $^{\circ}\text{C}$ (see Fig. 2) by regulated movement of barriers. The isotherms were repeated and there was fair reproducibility in measurements. The monolayer was transferred to RCA cleaned Si(001) substrate using horizontal deposition technique [21,22]. The pressure of the monolayer, at which the film is transferred was varied by choosing different compression regions as shown in the π - A isotherm (refer to Fig. 2). Here we present data of the films transferred at pressures of 2, 5, 10, and 14 mN/m. The dipper speed was 1 mm/min and barrier speed for both forward and backward direction was 1 mm/min. All the films were transferred at 18 $^{\circ}\text{C}$. One sample was transferred at 12 mN/m at same temperature to monitor real-time evolution of the monolayer using AFM.

XRR technique is a powerful, nondestructive probe to monitor the variations in the electron-density profile (EDP)

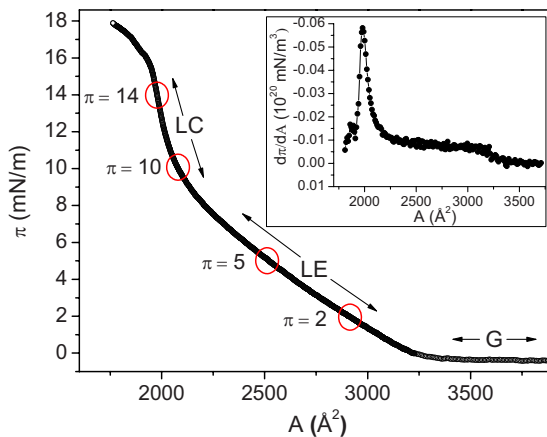


FIG. 2. (Color online) (π - A) isotherm recorded at the Langmuir trough showing various phases. Inset: corresponding derivative curve to emphasize the changes.

with respect to the depth (z) of a variety of systems ranging from crystalline to noncrystalline solids, liquid surfaces and interfaces [25,26]. It is known that XRR measurements carried out as a function of time [27] can provide information about instability in the sample. The XRR measurements of the films were carried out in a diffractometer (D8 Discover, Bruker AXS) with Cu source (sealed tube) followed by Göbel mirror to select and enhance Cu $K\alpha$ radiation ($\lambda=1.54$ \AA) to get average information of the film. The reflectivity is measured under specular conditions [incident angle (α)=exitangle(β)], where $q_z(=4\pi/\lambda \sin \alpha)$ is the only nonzero component of the wave vector (\mathbf{q}) and gives the out-of-plane information. The refractive index of a material in x-ray regime is slightly less than unity. There is a positive critical angle α_c (or a critical wave vector q_c) such that for any $\alpha \leq \alpha_c$ total external reflection occurs. The mathematical formalism based on electromagnetic theories that approximate the films as a stack of multiple homogeneous layers with infinitely sharp interfaces was developed by Parratt [28]. A modified formalism to include the effect of surface and interfacial roughness has been used here to analyze the reflectivity data. In this formalism the reflectivity as a function of q_z for a thin film of finite thickness d over a substrate, is given [26] as $R(q_z)=r_0 r_0^*$, where

$$r_0 = \frac{r_{1,2} + r_{2,3}}{1 + r_{1,2}r_{2,3}}, \quad (1)$$

with $r_{1,2}$ and $r_{2,3}$ being the reflectance for the vacuum-film and film-substrate interfaces respectively. The above calculation can be extended for M such thin stratified layers of thickness d_n and one arrives at a recursive formula in terms of Fresnel reflectance given by

$$r_{n-1,n}^F = \frac{r_{n,n+1} + F_{n-1,n}}{r_{n,n+1}F_{n-1,n} + 1} \exp(-iq_{n-1,z}d_{n-1}), \quad (2)$$

where

$$F_{n-1,n} = \frac{q_{n-1,z} - q_{n,z}}{q_{n-1,z} + q_{n,z}}. \quad (3)$$

In the n^{th} stratified layer the corresponding wave vector is defined as $q_{n,z}=(q_z^2 - q_{n,c}^2)^{1/2}$. The Fresnel reflectance for the interface between n^{th} and $(n-1)^{\text{th}}$ stratified layer is modified to include the roughness σ_n of the n^{th} stratified layer and one can finally write the reflectance of a rough surface as

$$r_{n-1,n} = r_{n-1,n}^F \exp(-0.5q_{n-1,z}q_{n,z}\sigma_n^2). \quad (4)$$

In general, the electron-density variation in a specimen is determined by assuming a model for the same and comparing the simulated profile with the experimental data. EDP is extracted from the fit [26]. XRR for the films reported here were initially measured at time intervals of few hours and finally at time intervals of few days. In our analysis we have used four such stratified layers including a layer of Silicon dioxide. The AFM (Nanoscope IV, Digital Instruments) measurements of the four samples were done long after deposition to ensure that the surface had stabilized. For one of the samples, deposited at high pressure (12 mN/m), successive AFM (NTEGRA scanning probe microscope, NT-MDT)

measurements were done soon after transfer to monitor the real-time evolution of the monolayer. The AFM measurements were done in the tapping mode using etched silicon or Si_3N_4 cantilevers to reduce vulnerability of the monolayer toward sticking to the tip and to avoid tip-induced movements.

III. RESULTS

The isotherm shown in Fig. 2 exhibits the existence of at least three phases. A phase of high compressibility which we call a liquid expanded (LE) phase starting after the gaseous phase (G), and another phase of low compressibility which we designate as a liquid condensed (LC) before the collapse of the monolayer. The derivative of the isotherm (inset of Fig. 2) shows clear distinction in the phases which are not so evident in the isotherm. The collapse (high-compressibility phase after LC) of the monolayer can be assumed to occur when the nanoparticles relax the strain imposed due to the moving barriers by flipping over to form bilayers because the excitation required for such movement is very small ($\approx k_B T$). It must be mentioned here that in case of π - A isotherms of encapsulated nanoparticles/nanoclusters which are essentially hydrophobic and float on the air-water interface, pure phases are difficult to identify. Mostly there are mixed phases which extend over certain area and the various regions in these mixed phases are different from each other in the ratio in which the phases are mixed (see Fig. 2). The compressed monolayer of particles floating on water are actually composed of various domains in LC state, LE state, and G state. According to Flory-Huggins theory [29] there is mixing of entropy in such a thermodynamic state when the entities involved are different from each other in some way. The surface equation of state for such systems has been worked out and it has been shown experimentally [29] that the π - A isotherm in such systems depend on the entropy mixing parameter, domain size, temperature, and of course the nature of the surfactants involved. The regions in the π - A isotherm closer to the G phase will have more tendency to behave like a gaseous phase, while those closer to the LE phase will have properties resembling the liquidlike phase. The same applies for the mixed LC phase too. It is imperative thus to investigate at least two regions of a particular mixed phase because the properties at these regions will vary appreciably. Two films were deposited from the LE phase ($\pi=2$ and 5 mN/m) and two from the LC phase ($\pi=10$ and 14 mN/m). For ease of reference we shall label them as LE- G ($\pi=2$ mN/m), LE ($\pi=5$ mN/m), LC-LE ($\pi=10$ mN/m), and LC ($\pi=14$ mN/m). One film was deposited at $\pi=12$ mN/m (LC-LE phase) to see the real-time evolution of the monolayer using successive AFM scans.

The AFM topographs of the four samples transferred from the trough corresponding to the various regions in the isotherm (see Fig. 3) show varying structures in the form of isolated or meandering clusters or labyrinthine interconnected nanoscale patterns adhering directly onto the substrate as a percolating monolayer. Differences in coverage and in patterns are also seen although they are essentially of the same thickness of about 5 nm (about one monolayer of nano-

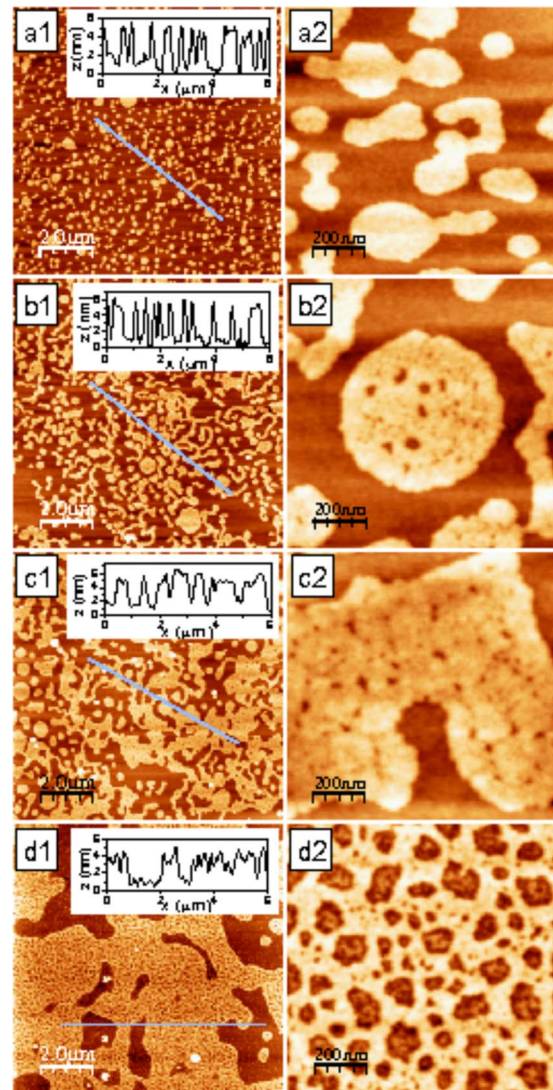


FIG. 3. (Color online) AFM topographs of the transferred films (a1-d1 for scan size $10 \times 10 \mu\text{m}^2$ and a2-d2 for scan size $1 \times 1 \mu\text{m}^2$) deposited at the four different pressures corresponding to different phases in the isotherm. a1 and a2 are the AFM images for LE- G phase, b1 and b2 for LE phase, c1 and c2 for LC-LE phase and d1 and d2 for LC phase. Insets of (a1-d1) show typical line profiles.

particles). The AFM image corresponding to the sample deposited from the LE- G phase ($\pi=2$ mN/m) has a low coverage (about 29%) and shows small, isolated clustered islands of nanoparticles of various sizes [see Fig. 3(a)1]. For all the samples the coverages have been calculated for at least five different areas (mostly from scans of higher areas $\sim 10 \times 10 \mu\text{m}^2$) and averaged upon to get a statistically meaningful value [30]. The islands also do not show any kind of patterns or holes within themselves even for higher magnification [see Figs. 3(a)1 and 3(a)2]. The AFM images for LE phase ($\pi=5$ mN/m) show better coverage (about 38%) than the LE- G phase with bigger islands having less intermittent space between themselves [Figs. 3(b)1 and 3(b)2]. Although at low magnification the image [Fig. 3(b)1] is similar to the image of the LE- G phase [Figs. 3(a)1

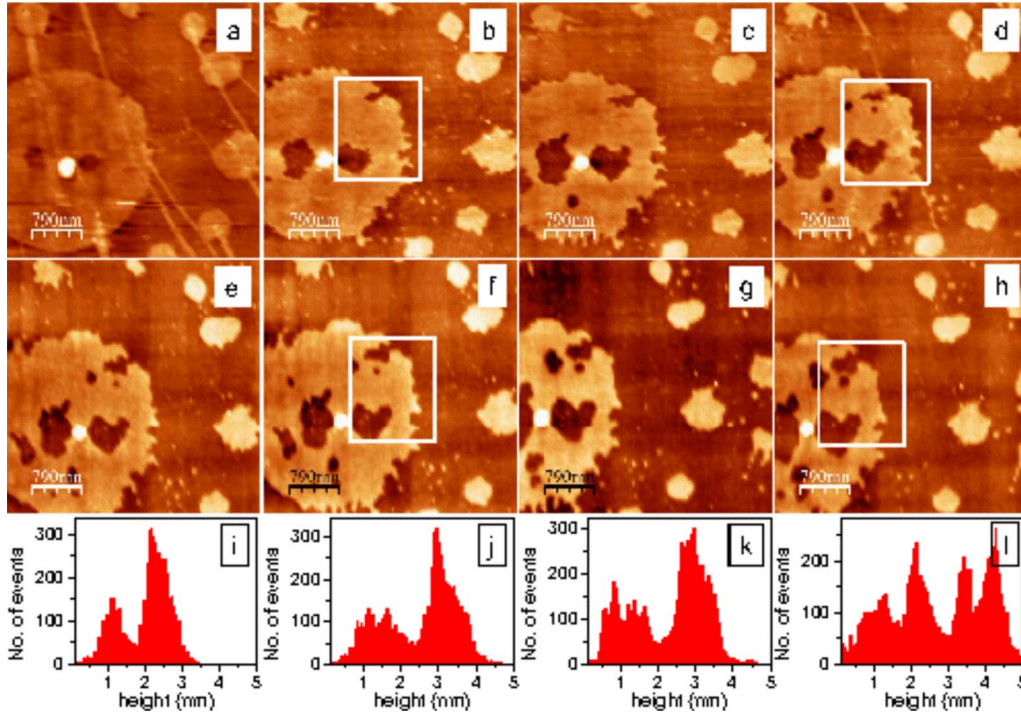


FIG. 4. : (Color online) (a)–(h) Successive AFM images (scan size $4 \times 4 \mu\text{m}^2$) of the film deposited at $\pi=12 \text{ mN/m}$ (corresponding to the LC-LE phase) taken every 30 min. (a) is after 30 min of deposition; (b)–(h) show images after 1, 1.5, 2, 2.5, 3, 3.5, and 4 h respectively. The small voids grow in dimension with time to give a patterned appearance to the island. (i-l) Typical height histograms of the images (b), (d), (f), and (h). The white boxes in b, d, f and h show the area from which the histograms have been calculated. The average height of the monolayer is seen to increase with time.

and 3(a)2], high magnification images show the presence of small pinholes which are very scarce in nature and scattered over the surface aperiodically [Fig. 3(b)2]. These holes were not observed for the LE-G phase. For the LC-LE phase (corresponding to a pressure of 10 mN/m) the coverage is greater (about 45%), large islands are seen to form and they are intricately knit with each other over a substantial area of the sample [see Figs. 3(c)1 and 3(c)2]. Small patterns are seen over the islands and higher magnification [Fig. 3(c)2] clearly shows that the holes (of the size up to 50 nm) are now more prominent and more abundant than before. Finally for the LC phase ($\pi=14 \text{ mN/m}$), we observe an appreciable coverage (about 62%) with the surface mostly occupied by the monolayer [Figs. 3(d)1 and 3(d)2]. Over the entire coverage, the islands show distinct patterns of cellular networks, more regular and more periodic in space having average dimension of about 120 nm. High magnification images show polygonal networks with defined edges [Fig. 3(d)2]. AFM images in Fig. 3 show only the final stage of evolution for all the samples. The set of AFM images shown in Fig. 4 however were done as a function of time to observe the real-time evolution of the monolayer transferred at the LC-LE phase ($\pi=12 \text{ mN/m}$). Figure 4(a) shows the circular islands just after transfer; Figs. 4(b)–4(h) show the tapping mode AFM images of the same scan area ($4 \times 4 \mu\text{m}^2$) taken after almost every 30 min. Figures 4(i)–4(l) show the height distribution for the images taken every 1 h [Figs. 4(b), 4(d), 4(f), and 4(h)]. The height distribution were calculated around the island only to reduce the strength of the substrate peak not covered by nanoparticles. The peak around 1 nm in the

height histograms correspond to the Si substrate not covered by nanoparticles. We observe, small voids appearing in the compact islands which gradually grow in dimension with time. The height histogram at later times show that the average height of the nanoparticles increases with time [Figs. 4(i)–4(l)]. This suggests some out-of-plane restructuring as a function of time. The outer edge of the islands however remain pinned to the surface. It is also observed that the voids are formed and increase in size only for the larger islands (refer to Table I) but there are no voids in the smaller islands although their shape becomes distorted with time.

TABLE I. Parameters extracted from the time-resolved AFM scans. The percentage of voids and the average height of the monolayer have been estimated from the large island that shows changes in the morphology.

Time (h)	Voids (%)	Average height of monolayer (nm)
0.5	4	2.4
1	8	2.4
1.5	15	2.7
2	17	2.8
2.5	19	2.9
3	20	3.0
3.5	23	3.5
4	23	4.0

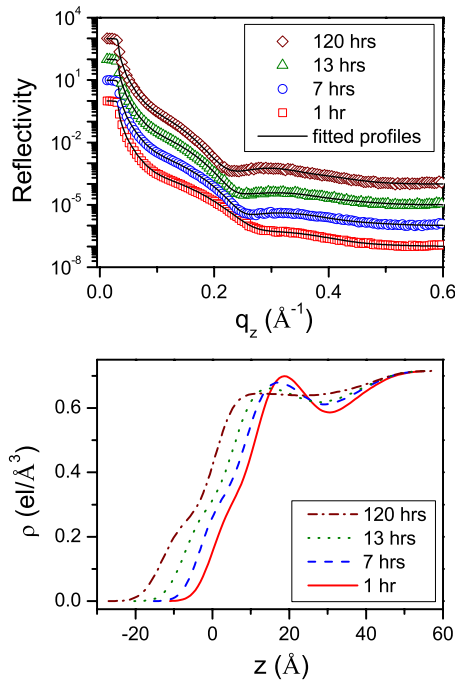


FIG. 5. (Color online) Time-evolution XRR profiles (scattered graphs) and the respective fits (solid lines) for the film transferred at $\pi=2$ mN/m. Lower panel shows the EDPs (obtained from convolution of AED of stratified layers with interfacial roughness) corresponding to the fits.

The XRR measurements which were done at frequent time gaps of hours initially and then at longer time gaps of days later on, show changes in their profiles (shift in the dip position toward the lower momentum-transfer (q_z) value) for all the films. The change is very small for the LE-G phase ($\pi=2$ mN/m) but increases for the more condensed phases and is appreciable for the film with maximum coverage (refer top panels in Figs. 5–8). The XRR profiles for all the samples were fitted [see Eq. (4)] using Parratt formalism [28] and the fitted profiles together with the EDPs derived from the fittings have been shown in lower panels of Figs. 5–8. In our model, three discretized stratified layers placed successively atop the silicon substrate (having a 20 Å native oxide layer) were used. The thicknesses of the bottom stratified layer, middle stratified layer and the topmost stratified layer are z_{th1} , z_{Au} , and z_{th2} , respectively, the average electron densities (AEDs) for them are ρ_{th1} , ρ_{Au} , and ρ_{th2} and the roughnesses are σ_{th1} , σ_{Au} and σ_{th2} . The values of the parameters used for fitting the XRR profiles for each film has been tabulated in Table II. The EDPs for all the samples show that the average thickness of the film increases slightly. The main contribution of the reflectivity comes from the Au core (Au being a strong scatterer) and the changes in the EDP of the film as a whole is dominated by the changes in the AED of the Au stratified layer. Figure 9 shows the schematics (as suggested by the variations in the EDPs for all the films) for the initial positions and the final positions after the out-of-plane variations of the nanoclusters have stabilized. The fluctuation in the monolayer is very small for the LE-G and the LE phase but is enhanced for the more condensed phases. It is high for the LC-LE phase and is maximum for the LC phase.

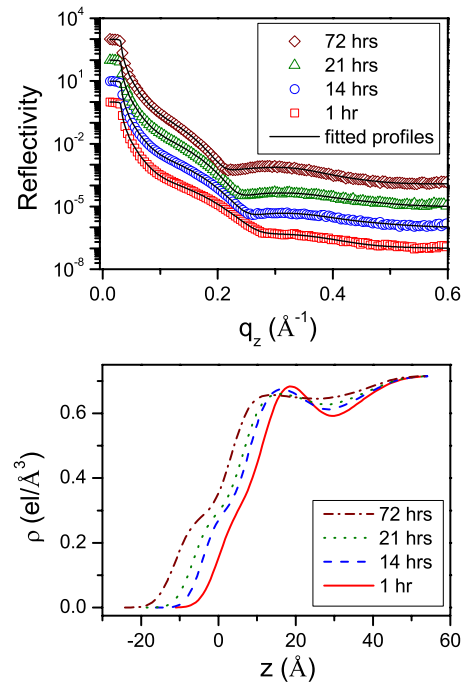


FIG. 6. (Color online) Time-evolution XRR profiles (scattered graphs) and the respective fits (solid lines) for the film transferred at $\pi=5$ mN/m. Lower panel shows the EDPs corresponding to the fits.

IV. DISCUSSION

There are various possibilities that can explain the observed phenomenon of patterning. We have considered the following mechanisms such as (1) spinodal decomposition or

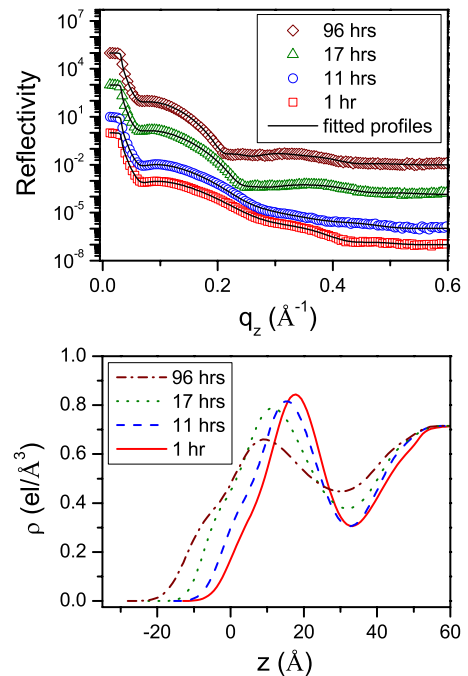


FIG. 7. (Color online) Time-evolution XRR profiles (scattered graphs) and the respective fits (solid lines) for the film transferred at $\pi=10$ mN/m. Lower panel shows the EDPs corresponding to the fits.

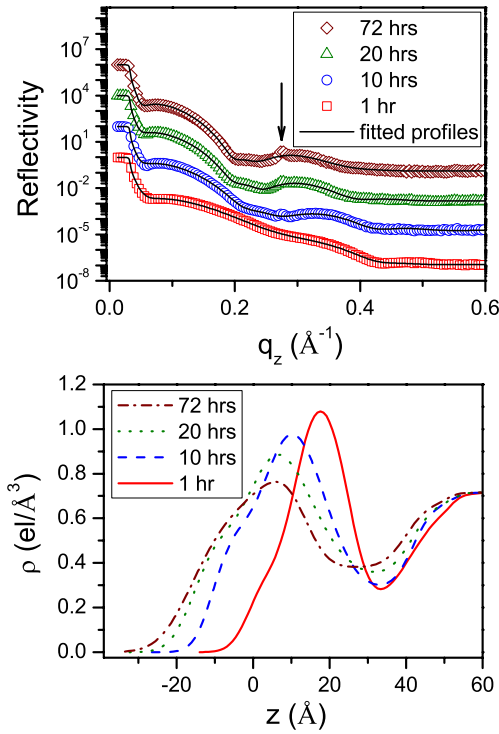


FIG. 8. (Color online) Time-evolution XRR profiles (scattered graphs) and the respective fits (solid lines) for the film transferred at $\pi=14$ mN/m. Lower panel shows the EDPs corresponding to the fits. The peaks in the XRR profiles of the sample (marked by arrow) may be due to some multilayered stacks formed at the edges of the film after drying.

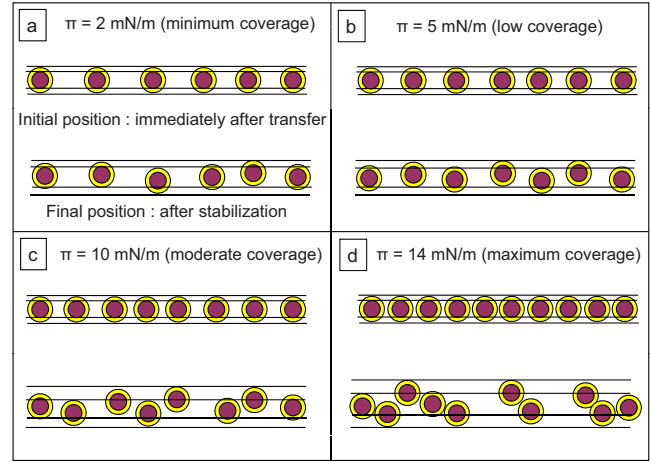


FIG. 9. (Color online) The schematics for the initial and the final positions (fluctuation in the monolayer) of the clusters in the film transferred at different pressures, derived from the respective EDPs. The relative fluctuation is very small in case of films corresponding to the mixed LE phases (a) and (b) but it is rather large for the films corresponding to the mixed LC phases (c) and (d).

dewetting, (2) contrarotatory hydrodynamic convection (Marangoni-Bénard convection), and (3) drying-mediated self-assembly. Spinodal decomposition and spinodal dewetting (seen in polymeric materials, homogeneous liquid metal films and liquid crystals) proceeds via dynamically unstable surface waves on the liquid surface and have strong dependence on the nature and magnitude of interfacial interactions [10]. In most cases, the sustaining mode grows and deter-

TABLE II. Different parameters, such as thickness (z), AED, and roughness (σ) obtained from the analysis of time evolution XRR data for the four samples transferred at different pressures. z_{th1} is the thickness of the first stratified layer after the substrate (having a native oxide layer of 20 Å and a roughness of 5.3 Å over it), ρ_{th1} is the corresponding AED and σ_{th1} the roughness. Similarly z_{Au} and z_{th2} are the thicknesses, ρ_{Au} and ρ_{th2} are AED's, and σ_{Au} and σ_{th2} are the roughnesses of the second and third stratified layer, respectively.

Pressure (mN/m)	Label	Time (h)	z (Å)			AED (el/Å ³)			σ (Å)		
			z_{th1}	z_{Au}	z_{th2}	ρ_{th1}	ρ_{Au}	ρ_{th2}	σ_{th1}	σ_{Au}	σ_{th2}
2	LE-G	1	12.1	13.8	10.6	0.53	0.68	0.28	2.7	4.5	3.0
		7	16.0	14.3	11.7	0.57	0.66	0.30	3.1	4.1	3.1
		13	17.9	14.4	12.5	0.59	0.65	0.27	2.2	4.6	3.2
		120	21.6	13.9	13.1	0.63	0.64	0.34	3.0	5.0	3.3
5	LE	1	12.2	12.6	12.2	0.53	0.68	0.28	3.5	4.4	3.0
		14	15.5	13.5	11.8	0.57	0.64	0.28	2.0	4.0	2.6
		21	17.8	14.0	12.6	0.59	0.63	0.26	2.2	4.5	2.9
		72	19.0	15.0	14.2	0.60	0.63	0.25	1.5	4.3	2.8
10	LC-LE	1	13.0	13.5	10.6	0.19	0.99	0.32	4.9	6.3	3.1
		11	16.4	13.8	10.7	0.26	0.88	0.41	5.0	4.3	3.2
		17	22.1	13.7	12.2	0.37	0.89	0.39	6.2	5.0	3.2
		96	24.4	14.5	13.3	0.45	0.71	0.45	3.6	8.2	6.4
14	LC	1	21.7	14.1	14.6	0.24	1.18	0.20	4.0	5.1	3.6
		10	24.2	13.1	14.8	0.26	1.12	0.53	6.2	5.3	3.7
		20	27.9	13.2	16.2	0.33	1.06	0.54	7.8	5.0	5.0
		72	28.0	13.0	16.4	0.41	0.85	0.57	4.6	7.5	6.6

mines the characteristic length scale of the dewetted structure. There has been reports of substrate strain-mediated spinodal decomposition to produce nanoscale patterning of a chemisorbed organic monolayer [13] and two-dimensional self-assembly of Au adatom gas on Au(111) surface via spinodal decomposition [12]. In case of transferred monolayers of nanoparticles, there can be dewetting effects during drying that cannot be ruled out. We however observe that the lateral movement of the clusters is much more than the transverse movement (Fig. 4). In the final structure, the height of the film increases only slightly and is much smaller than what is expected in case of dewetting effects. We can subsume that dewetting effects leading to the observed patterning here are less dominant.

The instability induced by contrarotatory hydrodynamic (Marangoni-Bénard) convections that leads to patterning, can be a possible mechanism here provided the Marangoni number exceeds a certain value. We have calculated Marangoni number given by $M_a = 8\alpha^2$, where $\alpha (=2\pi h/\lambda)$ is a dimensionless quantity. Here h is the height of the liquid and λ is the characteristic length of the patterns. M_a should have a value >80 for the onset of convection driven instability [8]. Considering the fact that we see patterns with a characteristic length ~ 100 nm, the height of the liquid (water) layer over which the nanoclusters float should be higher than 100 nm. We do not observe any decrement of height of the order of 100 nm in our AFM scans carried out as a function of time (Fig. 4) although sequential images show the evolution of the monolayer from circular disklike island to patterned island. The height of the liquid transferred along with the film and trapped in the islands must be very small, almost comparable to the thickness of the nanoclusters. Assuming $h \leq 5$ nm and $\lambda \sim 100$ nm we find $M_a \approx 0.8$. The value to M_a is extremely small for such small liquid height and there cannot be any onset of Marangoni convection which can induce instability in the monolayers.

The observed patterning has strong similarity with the simulated patterns generated from a model Hamiltonian that exploit nucleation and growth of voids or holes [1] during late stage of drying. The Hamiltonian can be written as [1,31]

$$H = -\epsilon_l \sum_{\langle ij \rangle} l_i l_j - \epsilon_n \sum_{\langle ij \rangle} n_i n_j - \epsilon_{nl} \sum_{\langle ij \rangle} n_i l_j + \mu(\nu) \sum_i l_i, \quad (5)$$

where ϵ_l , ϵ_n , and ϵ_{nl} are the energies of liquid-liquid, nanoparticle-nanoparticle, and nanoparticle-liquid interactions. A lattice site i is either occupied by liquid state ($l_i = 1$) or vapor state ($l_i = 0$) or by a nanoparticle ($n_i = 1$). The chemical potential (μ) (which is a function of the fraction of solvent in the vapor state given by ν) governs the dynamical state of the system. A nanoparticle can only move if the site to which it moves is filled with liquid and also the energy required for such movement (determined by the Metropolis algorithm) is acceptable. When the evaporation is heterogeneous in nature, complex patterns are formed due to growth and nucleation of holes which carry the mobile nanoparticles on their advancing outer fronts. As more liquid leaves the surface the holes grow in dimension until the nanoparticles are stationed at the boundaries of adjacent holes leading to

networklike patterns. The movement of the nanoparticles is frozen once the liquid has dried up and the instability in the film is then stabilized. The experimentally observed length scales of patterns presented are similar to the length scales obtained from simulation studies [32] involving the above Hamiltonian. For $\mu/\epsilon_l = 2.5$, $k_B T/\epsilon_l = 0.3$, $\epsilon_n/\epsilon_l = 1.5$, and $\epsilon_{nl}/\epsilon_l = 2$, at about 60% coverage, the characteristic length of patterns match very well with our results. The characteristic length of patterns in this simulation work is determined by the interplay of the time scale of evaporation of the liquid and the time scale of diffusion of nanoparticles [1,31]. It has been reported that a transition from patterning caused by nucleation and growth to that caused by spinodal dewetting occurs when the value of $k_B T/\epsilon_l$ is around 0.3. Above this value the dynamic chemical potential assumes a sigmoidal form leading to observation of multiple-scale pattern morphology, nanoparticle rings, viscous fingerings and fractals [32]. The simulated patterns which match with the experimentally observed patterns here, fall within the regime of patterning by nucleation and growth of holes. However for low coverage films, the patterns observed here do not match with simulated patterns. The cluster size as well as the number and size of pinholes is seen to increase with coverage. It must be noted that the outer periphery of the islands however does not move and is pinned to the surface. The in-plane as well as out-of-plane displacement of the nanoclusters, is assumed to be only within the boundary of the islands (see Fig. 4). The EDP extracted from the XRR measurements (refer to Figs. 5–8) show that the average height of the nanoparticles increases but the AED decreases as the liquid evaporates with time. The increase in the average height of the film is also seen by height histogram obtained from AFM measurements (Fig. 4) carried out sequentially after deposition to substrate.

It is known that during the process of spreading the nanoparticles on the water layer in the trough, clusters are formed due to coalescence of nanoparticles by kinetically governed self-assembly [15]. During further compression the number of such clusters per unit area (coverage as well as the interconnectivity) increases as the nearest-neighbor distance of the nanocrystals among themselves and with that of the perimeter of an island already formed by such coalescence decreases [16]. The barriers are compressed to attain the target pressure and the unstable monolayer with trapped water is transferred to the substrate. AFM images for the LE-G phase show the presence of a large number of isolated small clusters [Figs. 3(a)1 and 3(a)2] and the AFM images of the samples deposited at higher pressures [Figs. 3(b)1 and 3(b)2 for $\pi = 5$ mN/m, Figs. 3(c)1 and 3(c)2 for $\pi = 10$ mN/m, and Figs. 3(d)1 and 3(d)2 for $\pi = 14$ mN/m] exhibit larger clusters.

XRR measurements and analysis (refer to Figs. 5–8) clearly show that instability in the monolayer makes the film thicker during the late stage of drying and dip position at $q_z = 0.3 \text{ \AA}^{-1}$ shifts toward lower value. This shift in the dip position of the XRR profiles is more for the more condensed phases. The EDPs show that there are fluctuation in the structure of the monolayer for all the samples for initial 20–30 h. The fluctuations are much higher in case of the high coverage films ($\pi = 10$ and 14 mN/m) as compared to the low

coverage films ($\pi=2$ and 5 mN/m). The change in the thicknesses and the AEDs of the individual stratified layers used to model the system (see Table I) suggest that the out-of-plane restructuring of the monolayer is very small in $\pi=2$ and 5 mN/m, moderate in $\pi=10$ mN/m and prominent for $\pi=14$ mN/m. The EDPs for all the films show an increase in the thickness (which is also evidenced by AFM imaging carried out as a function of time, shown in Fig. 4) but decrease in the AED although the area under the EDP is almost constant. So the possibility of adsorption/desorption to/from the film can be ruled out during drying process. This is also suggestive of the fact that the Au particles do not stay with their center of mass in the same line but shift up/down with respect to each other as transferred water gradually leaves the substrate surface through the islands. The extracted information from XRR analysis is shown as a model in Fig. 9 to demonstrate the initial and final structure of the monolayer as it stabilizes with time. The EDPs for $\pi=2$ and 5 mN/m and the associated parameters used for fitting the XRR profiles are similar. The instability in the monolayer for the LE-G phase and the LE phase, mainly consisting of rarefied small clusters is evident but weak and there are no patterns [see Figs. 3(a)1, 3(a)2, and Figs. 3(b)1 and 3(b)2]. The EDPs for the LC-LE phase shows more coverage and more displacement of the material. The AEDs of the top and bottom stratified layers increase while that of the middle stratified layer decreases. The particles however cannot move downwards beyond a certain value because of the presence of rigid substrate, so the dominating part is the fraction of the particles that move upward from their initial position. AFM images [Figs. 3(c)1 and 3(c)2] show widened pinholes which are now abundant, giving the islands a perforated look. Finally, the EDPs for the LC phase show the same trend as the LC-LE phase but the instability and consequently the fraction of material movement is more. AFM images [Figs. 3(d)1 and 3(d)2] show that well-developed patterns with defined edges have indeed formed over the entire film. For the LC phase there is a peak in the XRR profile (marked by arrow in Fig. 8) which might be due to the presence of some multilayers at the edges of the sample after drying. XRR measurements were done around the peak in finer steps. The sample

was shifted up/down with respect to the x-ray beam to probe the edges. The peak was prominent when the irradiated area was at the edges and the peak vanished when the XRR was collected from the middle of the sample. This however bears less significance toward the patterning mechanism in the transferred films. Thus patterning is seen only for high coverage films ($\pi=10$ and 14 mN/m) corresponding to the mixed LC phases (with large interconnected clusters) where the fluctuation in the monolayer is quite large in comparison to the low coverage films ($\pi=2$ and 5 mN/m).

V. CONCLUSION

We have investigated the evolution in the structure and morphology of the transferred monolayer by two complementary techniques viz. AFM and XRR. The evolution observed here is brought about by drying-mediated self-assembly of nanoparticles. The aggregation into clusters happens as the particles lay floating on the air-water interface once the solvent in which the nanoparticles are dispersed evaporates, the coalescence happens when the film is compressed to attain a desired phase from which the film is transferred onto the substrate and the patterning happens at a late stage of drying when the liquid trapped underneath the islands evaporates through them. The mechanism behind the patterning is mainly due to the drying-mediated self-assembly where the particles are driven by the advancing fronts of the voids or holes and pushed to the boundaries of similar adjacent voids created by the heterogeneously evaporating liquid. Time-resolved AFM scans show the clear evidence of the evolution in the structure of the nanoparticle monolayer and is well supported by XRR measurements taken as a function of time. We thus infer that by having a precise control over the film preparation criteria (such as surface pressure of deposition, temperature and concentration of nanoparticles in the aliquot), one can perhaps choose the prerequisite of self-assembly which can then be exploited for nanodevice fabrication. However, there are certain factors such as deposition temperature and humidity conditions that change the drying process and affect pattern formation mechanism significantly and need to be investigated further.

-
- [1] E. Rabani, D. R. Reichman, P. L. Geissler, and L. E. Brus, *Nature (London)* **426**, 271 (2003).
 [2] R. P. Andres, J. D. Bielefeld, J. I. Henderson, D. B. Janes, V. R. Kolagunta, C. P. Kubiak, W. J. Mahoney, and R. G. Osifchin, *Science* **273**, 1690 (1996).
 [3] C. B. Murray, C. R. Kagan, and M. G. Bawendi, *Annu. Rev. Mater. Sci.* **30**, 545 (2000).
 [4] P. Alivisatos, *Pure Appl. Chem.* **72**, 3 (2000).
 [5] J. N. Israelachivilli, *Intermolecular and Surfaces Forces*, 2nd ed. (Academic, New York, 1992).
 [6] B. A. Korgel and D. Fitzmaurice, *Phys. Rev. Lett.* **80**, 3531 (1998).
 [7] H. Bénard, *Rev. Gen. Sci. Pures Appl.* **4**, 489 (1900).
 [8] M. Maillard, L. Motte, A. T. Ngo, and M. P. Pileni, *J. Phys. Chem. B* **104**, 11871 (2000).
 [9] V. X. Nguyen and K. J. Stebe, *Phys. Rev. Lett.* **88**, 164501 (2002).
 [10] S. Herminghaus, K. Jacobs, K. Mecke, J. Bischof, A. Fery, M. Ibn-Elhaj, and S. Schlagowski, *Science* **282**, 916 (1998).
 [11] P. Moriarty, M. D. R. Taylor, and M. Brust, *Phys. Rev. Lett.* **89**, 248303 (2002).
 [12] R. Schuster, D. Thron, M. Binetti, X. Xia, and G. Ertl, *Phys. Rev. Lett.* **91**, 066101 (2003).
 [13] K. S. Schneider, W. Lu, T. M. Owens, D. R. Fossnacht, M. M. Banaszak Holl, and B. G. Orr, *Phys. Rev. Lett.* **93**, 166104 (2004).
 [14] G. Gu and L. Brus, *J. Phys. Chem. B* **12**, 207 (2000).
 [15] T. P. Bigioni, X.-M. Lin, T. T. Nguyen, E. I. Corwin, T. A.

- Whitten, and H. M. Jaeger, *Nature Mater.* **5**, 265 (2006).
- [16] C. P. Martin, M. O. Blunt, and P. Moriarty, *Nano Lett.* **4**, 2389 (2004).
- [17] S. Pal, N. S. John, P. J. Thomas, G. U. Kulkarni, and M. K. Sanyal, *J. Phys. Chem. B* **108**, 10770 (2004).
- [18] S. Pal, M. K. Sanyal, N. S. John, and G. U. Kulkarni, *Phys. Rev. B* **71**, 121404(R) (2005).
- [19] M. K. Bera, M. K. Sanyal, S. Pal, J. Daillant, A. Datta, G. U. Kulkarni, D. Luzet, and O. Kononov, *EPL* **78**, 56003 (2007).
- [20] J. K. Basu, S. Hazra, and M. K. Sanyal, *Phys. Rev. Lett.* **82**, 4675 (1999).
- [21] A. Datta, S. Kundu, M. K. Sanyal, J. Daillant, D. D. Luzet, C. Blot, and B. Struth, *Phys. Rev. E* **71**, 041604 (2005).
- [22] S. Kundu, A. Datta, and S. Hazra, *Langmuir* **21**, 5894 (2005).
- [23] M. Brust, M. Walker, D. Bethell, D. J. Schiffrin, and R. Whyman, *Chem. Commun. (Cambridge, U.K.)* (1994) 801.
- [24] W. P. Halperin, *Rev. Mod. Phys.* **58**, 533 (1986).
- [25] M. Tolan, *X-Ray Scattering from Soft Matter Thin Films* (Springer, Berlin, 1999); *X-Ray and Neutron Reflectivity: Principles and Applications*, edited by J. Daillant and A. Gibaud (Springer, Paris, 1999).
- [26] J. K. Basu and M. K. Sanyal, *Phys. Rep.* **1**, 363 (2002).
- [27] J. K. Bal and S. Hazra, *Phys. Rev. B* **75**, 205411 (2007).
- [28] L. G. Parratt, *Phys. Rev.* **95**, 359 (1954).
- [29] E. Ruckenstein and B. Li, *J. Phys. Chem. B* **102**, 981 (1998).
- [30] I. Horcas, R. Fernández, J. M. Gómez-Rodríguez, J. Colchero, J. Gómez-Herrero, and A. M. Baro, *Rev. Sci. Instrum.* **78**, 013705 (2007).
- [31] C. P. Martin, M. O. Blunt, E. Pauliac-Vaujour, A. Stannard, P. Moriarty, I. Vancea, and U. Thiele, *Phys. Rev. Lett.* **99**, 116103 (2007).
- [32] A. Stannard, C. P. Martin, E. Pauliac-Vaujour, P. Moriarty, and U. Thiele, *J. Phys. Chem. C* **112**, 15195 (2008).